Three-dimensional macroporous nanoelectronic networks as minimally invasive brain probes

Chong Xie[1†], Jia Liu[1†], Tian-Ming Fu[1†], Xiaochuan Dai[1], Wei Zhou[1] and Charles M. Lieber[1,2]★

Direct electrical recording and stimulation of neural activity using micro-fabricated silicon and metal micro-wire probes have contributed extensively to basic neuroscience and therapeutic applications; however, the dimensional and mechanical mismatch of these probes with the brain tissue limits their stability in chronic implants and decreases the neuron–device contact. Here, we demonstrate the realization of a three-dimensional macroporous nanoelectronic brain probe that combines ultra-flexibility and subcellular feature sizes to overcome these limitations. Built-in strains controlling the local geometry of the macroporous devices are designed to optimize the neuron/probe interface and to promote integration with the brain tissue while introducing minimal mechanical perturbation. The ultra-flexible probes were implanted frozen into rodent brains and used to record multiplexed local field potentials and single-unit action potentials from the somatosensory cortex. Significantly, histology analysis revealed filling-in of neural tissue through the macroporous network and attractive neuron–probe interactions, consistent with long-term biocompatibility of the device.

At present, there is intense interest in the development of materials and electronic devices that can extend and/or provide new capabilities for probing neural circuitry and afford long-term minimally invasive brain–electronics interfaces[1–4]. Conventional brain probes have contributed extensively to basic neuroscience[5,6] and therapeutic applications[7–10], although they suffer from chronic stability and poor neuron–device contacts[4,11–13]. Recent studies of smaller[14,15] and more flexible[16,17] probes suggest that addressing size and mechanical factors could help overcome current limitations.

The most common neural electrical probes are fabricated from metal[18] and silicon[19,20], materials that have very different structural and mechanical properties from those of brain tissue[21]. Evidence suggests that mechanical mismatch is an important reason leading to abrupt and chronically unstable interfaces within the brain[4,22]. For example, motion of skull-affixed rigid probes in chronic experiments can induce shear stresses and lead to tissue scarring[13,23], thereby compromising the stability of recorded signals on the timescale of weeks to months[4,24,25]. More recent work has shown that flexible probes fabricated on polymer substrates[12,17] and smaller-sized probes[11,14] can reduce deleterious tissue response. More generally, there has also been effort developing flexible bioelectronics[26–28] and nanoscale devices for single-cell recording[29,30]. We have also shown that three-dimensional (3D) macroporous electronic device arrays can function as scaffolds for and allow 3D interpenetration of cultured neuron cell networks without an adverse effect on cell viability[31], and such networks can be injected by syringe through needles into materials, including brain tissue[32]. In the latter case, it remains challenging to make the electrical input/output (I/O) connections needed for recording signals as the conventional I/O cannot pass through the injection needles.

Taking the above facts into consideration, we define an ideal implantable neural probe as possessing a stiffness similar to brain tissue to minimize/eliminate mechanically induced scarring, a high degree of porosity and cellular/subcellular feature sizes to allow interpenetration and integration of neurons and neural projections with the electronics, a means for implantation of the resulting extremely flexible structure, and facile I/O to allow multiplexed recording. Our strategy to meet these constraints focuses on implementing 3D macroporous nanoelectronic networks[31,33], where the macroporous nanoelectronic probe has a mesh-like structure designed to promote interpenetration and close integration with neural tissue (Fig. 1a,b). The mesh design is unique in having a two-dimensional (2D) open area of about 80%, feature sizes to sub-10 μm scale, and, importantly, a high flexibility with an effective bending stiffness of $<0.64 \times 10^{-15}\,\mathrm{N\,m^2}$ (Supplementary Information) four to seven orders of magnitude smaller than conventional Si (ref. 34), carbon fibre[14] and thin polyimide[16,35] neural probes. The exceptionally small bending stiffness yields mechanical interactions with tissue in the range of cellular forces. For instance, the force to deflect the two sensor-supporting arms by 10 μm (scale of a cell) is estimated to be about 10 nN, which is comparable to the single-cell migration force[36] (Supplementary Methods).

Our fabrication exploits conventional planar 2D lithography with a sacrificial layer that is etched to yield the free-standing macroporous nanoelectronic probe (Fig. 1c). The overall design of the mesh probe (Fig. 1c, Supplementary Fig. 1 and Supplementary Table 1) consists of longitudinal metal interconnects that are sandwiched between SU-8 polymer layers for passivation and transverse SU-8 polymer structural elements. In addition, transverse compressive strain elements are incorporated to generate positive transverse curvature and yield a cylindrical global probe structure, and local tensile strain elements in the supporting arms of each sensor device are incorporated to produce negative curvature, bending the devices away from the surface of the cylinder. All key materials and feature sizes of the macroporous nanoelectronic probe are summarized in Supplementary Table 1. Facile I/O between the probe and measurement electronics is achieved by bonding a printed circuit board (PCB) connector to the remaining portion

[1]Department of Chemistry and Chemical Biology, Harvard University, Cambridge, Massachusetts 02138, USA. [2]John A. Paulson School of Engineering and Applied Sciences, Harvard University, Cambridge, Massachusetts 02138, USA. †These authors contributed equally to this work.
*e-mail: cml@cmliris.harvard.edu
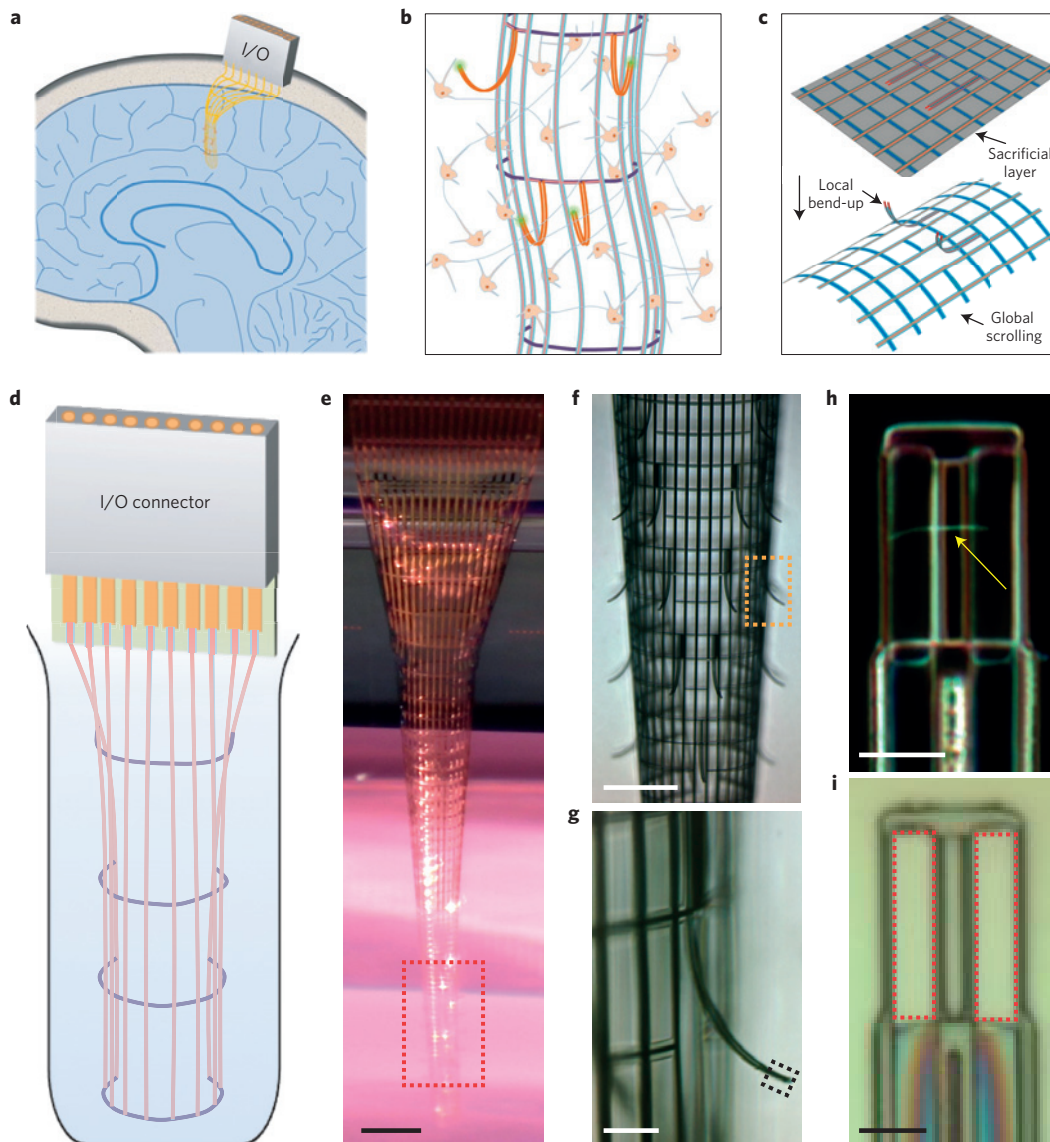
Figure 1 | Macroporous nanoelectronic 3D neural probes. a, Schematic of the probe implanted in the brain. The macroporous and flexible probe (yellow lines) is implanted in the brain and connected to the cranially mounted I/O connector. **b**, Schematic of the microscopic interface of the macroporous nanoelectronic brain probe with the neural circuit. The probe is constructed of polymer-encapsulated metal interconnecting and supporting elements (pink, purple and light blue), and arms (orange) that support and connect sensors (green). **c**, Schematic of the mechanism of probe geometry controlled by built-in strain after the removal of the sacrificial layer (grey). Compressive strain elements (transverse blue lines) shape the probe into a cylindrical structure. Tensile strain elements (red lines) cause the sensor-supporting arms to bend outwards from the probe surface. **d**, Schematic of an assembled macroporous probe with an I/O connector. The front end of the probe (pink lines) is suspended in buer and the back end (orange pads) is attached to a carrier substrate and connected to the I/O connector. **e**, Photograph of a typical macroporous nanoelectronic brain probe suspended in buffer with a cylindrical shape. Its back end is attached to the carrier substrate (the dark piece in the back) at the top of the image. Scale bar, 500 µm. **f**, Micrograph of the sensor area of the probe outlined by the red dashed box in **e**. The self-organization of the probe geometry, including global scrolling and outward bent supporting arms are visible. Scale bar, 200 µm. **g**, Zoomed-in view of the outward bent supporting arm and sensor outlined by the yellow dashed box in **f**. The black dashed box highlights the sensor element. Scale bar, 50 µm. **h**, Dark-field micrograph of a typical nanowire FET voltage sensor at the end of the supporting arms. The arrow points at a nanowire as the sensor unit. Scale bar, 5 µm. **i**, Bright-field micrograph of two typical Pt electrode voltage sensors each with 4 µm × 20 µm area. Scale bar, 5 µm.

of the substrate attached to the free-standing macroporous probe following fabrication (Fig. 1d and Supplementary Fig. 2a).

The macroporous probes were fabricated on standard silicon wafers with a nickel release layer using photolithography for multi-layer patterning (Supplementary Methods and Supplementary Fig. 2). Optical images at various resolutions of a representative probe structure before etching the nickel release layer (Supplementary Fig. 2) highlight all key probe features: the entire probe structure bonded to the PCB interface connector (Supplementary Fig. 2a);

the portion of the probe supported on the Ni layer and the silicon wafer that remains bonded to the PCB (Supplementary Fig. 2b); the lower part of the probe that will be released from the substrate and the overall locations of 19 sensor elements in this probe design (Supplementary Fig. 2c); and images of several addressable sensor elements, including one specific nanowire detector (Supplementary Fig. 2d,e).

Significantly, optical images of the probe structure following removal of the sacrificial nickel layer and underlying wafer (see
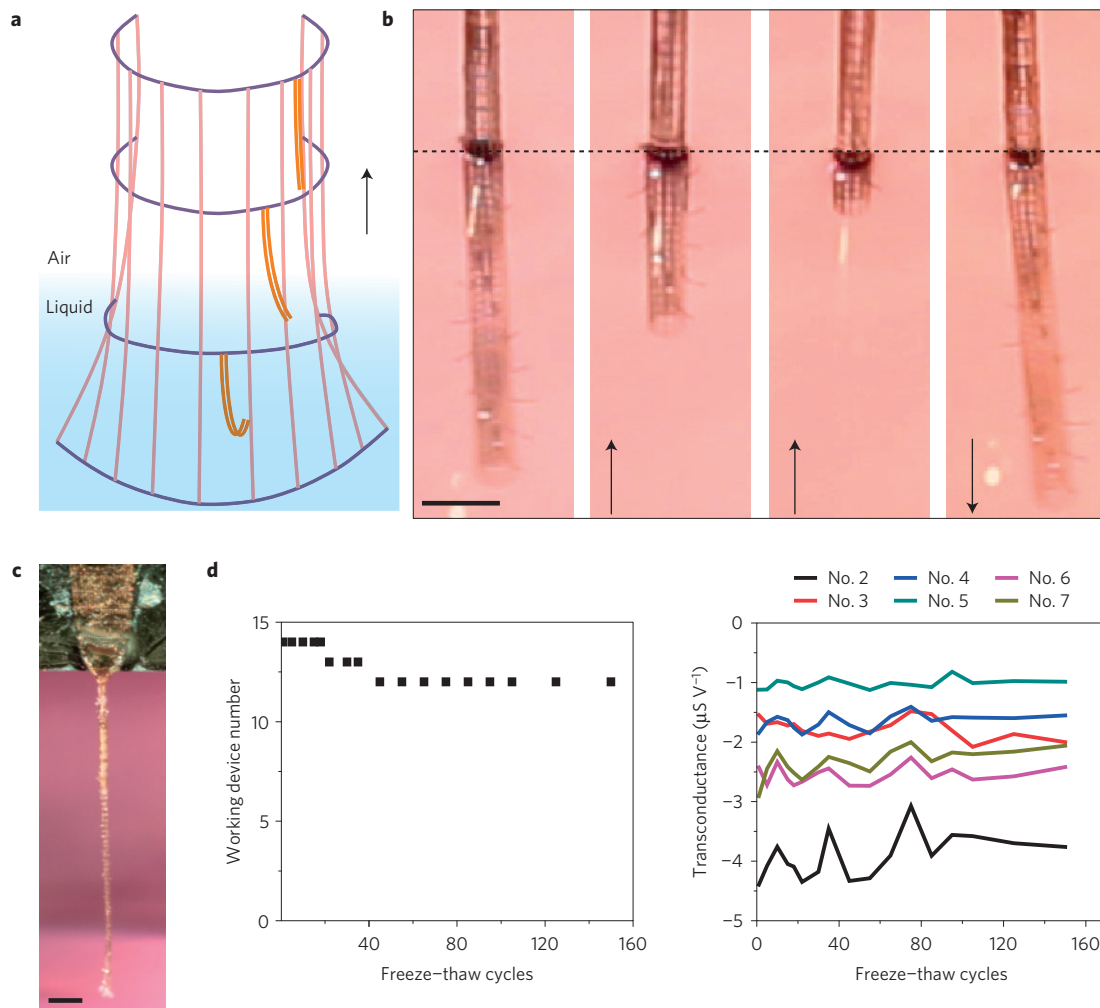
Figure 2 | Probe preparation and robustness. a, Schematic of the probe geometry control before implantation. The global curvature of the probe increases and the supporting arms are flattened as the probe is pulled from liquid to air. **b**, Four time-lapse images of the probe front-end geometry while it was moving in and out of the buffer. The dashed line marks the buffer surface (air above; buffer below). The black arrows indicate the direction of motion. Scale bar, 200 μm. **c**, Photograph of the probe in the 'frozen' state held in air by the carrier substrate. Scale bar, 500 μm. **d**, Sensor yield test following liquid nitrogen freezing and room-temperature thaw cycles. Left: Number of active nanowire FET sensors versus freeze–thaw cycle number. Right: Nanowire FET transconductance versus cycle number for 6 out of the 14 sensor elements.

Methods and Supplementary Methods), and immersion of the free-standing portion in aqueous buffer (Fig. 1e–i), highlight key features of our design. First, lower-resolution images (Fig. 1e) show that the transverse compressive strain elements produce self-organization of the probe into a global cylindrical shape as designed. This cylindrical geometry distributes the electronic sensor elements around the probe surface. Second, higher-resolution images (Fig. 1f,g) demonstrate that the local tensile strain introduced in the supporting arms of each sensor element bends these arms outwards such that each of the sensor elements is about 100 μm away from the cylindrical probe surface. The average leakage impedance of the SU-8-encapsulated metal interconnect components (Supplementary Fig. 3) was >10 GΩ at relevant frequencies, which demonstrates the effectiveness of the SU-8 passivation used in the probes. For sensor elements, we have incorporated either silicon nanowire field-effect transistors (FETs, Fig. 1h) or micrometre-scale platinum metal electrodes (Fig. 1i) into our probes during fabrication (see Methods and Supplementary Methods). Characterization of device performance and neural recording with these different sensor elements are discussed below.

The high flexibility of our macroporous probes precludes direct insertion[14,20] into neural tissue, and invasive surgery, which could allow placement of macroporous probes in specific brain regions, would largely eliminate many potential advantages of our design. To overcome this conundrum, we exploited the combination of built-in strain and liquid surface tension as probes are moved from liquid to air, as shown schematically in Fig. 2a and Supplementary Fig. 4. Specifically, on withdrawing probes from liquid to air, liquid surface tension increases the global curvature to yield straight cylinders with diameters of about 100–200 μm (Fig. 2b and Supplementary Movie 1). In addition, surface tension causes the supporting arms of the sensors to be 'pulled back' to yield a smooth probe surface on moving from liquid to air. Notably, the supporting arms return to the outward bent position with the sensors away from the probe surface when the probe is returned to an aqueous environment (Fig. 2b and Supplementary Movie 2). We recently reported a syringe injection approach for 2D mesh structures, although in this case all I/O connections must be introduced after injection.

This cylindrical probe structure has mechanical advantages compared to a flat structure, and although it remains too soft to penetrate brain tissue as removed from solution, rapid freezing in liquid nitrogen (Fig. 2c) provides sufficient rigidity to allow controlled insertion into hydrogel that has mechanical properties similar to dense neural tissue[37]. In particular, rapid insertion of the
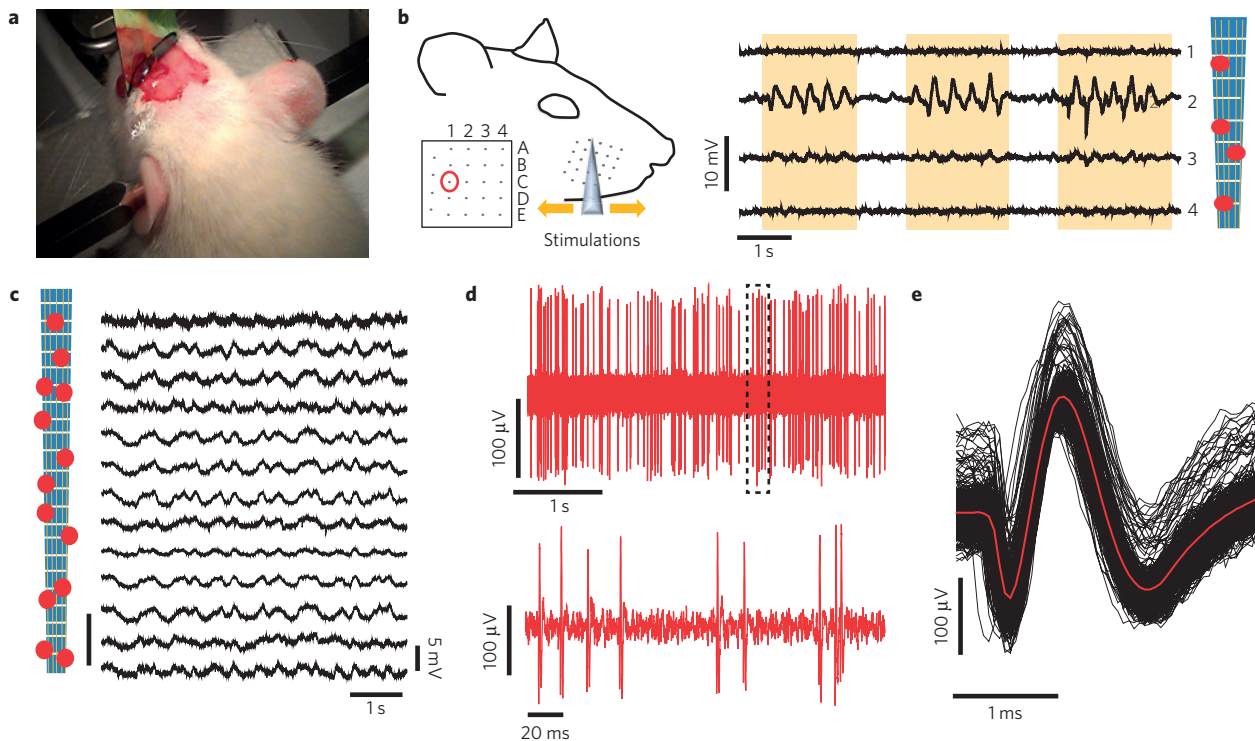
Figure 3 | Neural activity recording from rodent models. a, Photograph of a typical rodent stereotaxic surgery. A rat was held in a stereotaxic frame, and a macroporous nanoelectronic probe was implanted into the brain through a cranial hole. The probe was attached to the carrier substrate for external electrical connections (Supplementary Methods). **b**, Acute LFP recording by nanowire FET sensors from the barrel cortex area. Left: Schematic of the correlation between the neural activity in the barrel cortex and the rat whisker sensory behaviour. Inset: Schematic map of sub-areas in the barrel cortex. The red circle indicates the targeted sub-area. Right: Traces from four neighbouring sensors, where yellow areas mark stimulations applied to the whisker C1. Relative positions of the four sensors are marked in the schematic on the right. Scale bar, 200 μm. **c**, Acute multiplexed LFP recording from 13 nanowire FET sensors following probe insertion into the somatosensory cortex. Relative positions of the 13 sensors are marked in the schematic on the left. Scale bar, 200 μm. **d**, Top: Representative acute single-unit recording from Pt electrode sensors. Bottom: Zoomed-in view of nine single-unit events outlined in the top panel. **e**, Superimposed 94 single-unit events from the recording in **d**. The mean waveform of all traces is plotted in red.

frozen probe into 0.5% agarose gel (Supplementary Fig. 5) yields an extended configuration >2 mm into the hydrogel, whereas an unfrozen probe would simply be deformed at the gel surface without penetration. To determine whether freezing could be a reliable insertion and measurement strategy, we also studied the electrical performance of fully assembled probes when subjected to repeated cycles of exposure to liquid nitrogen freezing and room-temperature aqueous solution. Significantly, characterization of a nanowire FET-based probe following 150 freeze/thaw cycles (Fig. 2d) showed that 12 out of 14 (86%) FET sensors on the probe remained connected, and that 14/14 devices remained active up to 21 cycles. In addition, the device sensitivities showed <14% change on average after the 150 cycles, thus confirming the reliability of this approach. The observed robustness of the FET sensors is particularly encouraging because each device requires continuity of two interconnect lines, versus a single line for metal electrode sensors.

We have implanted the macroporous nanoelectronic probes in rodents. In a typical implantation procedure (Fig. 3a), the frozen macroporous probe is stereotaxically positioned and rapidly inserted to a specific region of the brain of an anaesthetized rodent (Methods). The positioning and inserting processes are kept within about 10 s and 1 s, respectively, to ensure successful insertion (Supplementary Fig. 4). Images recorded post-insertion (Supplementary Fig. 6a) highlight the high flexibility of our macroporous probe outside the brain, which allows positioning without moving the implanted portion within the tissue. In addition, a representative bright-field microscopy image of a post-insertion fixed tissue sample sectioned along the longitudinal axis of the probe

(Supplementary Fig. 6b) verifies an extended linear structure within the brain tissue.

We have exploited the capability to target specific brain regions via stereotaxic insertion of the frozen macroporous nanoelectronic probes to test their *in vivo* recording capabilities in rodents, where all of the reported measurements are acute and performed within 0.5–2 h post-implantation. First, a probe was implanted in the barrel cortex area of the rat brain as it represents a somatosensory cortex region with well-defined mapping between cortical columns and facial whiskers[38]. Signals recorded from four nanowire FET sensors showed strong signals in element-2 (6.3 ± 0.4 mV), corresponding to separate stimulations applied to the whisker C1 on the contralateral side of the implantation site (Fig. 3b), which was identified as the corresponding whisker by testing all whiskers (Supplementary Fig. 5). In contrast, the neighbouring FET sensor element-3 recorded a similar but much weaker signal pattern, whereas element-1 and -4, which are about 200 and 250 μm, respectively, from element-2, yielded no observable response.

Second, acute recording experiments made in the somatosensory cortex of an anaesthetized rat (Fig. 3c) demonstrate the capability for larger-scale multiplexed recording with the macroporous nano-electronic probes. Specifically, we recorded signals (3.4 ± 0.3 mV) simultaneously from 13 nanowire FET sensors on a single probe. The relatively large signal amplitude compared with that recorded by metal electrode sensors (typically <0.5 mV) is attributed to the active sensing nature of the FET sensors, which do not suffer from signal loss by shunt pathways[39]. The dominant modulation frequency, 1–4 Hz, is characteristic of δ-wave local field potentials
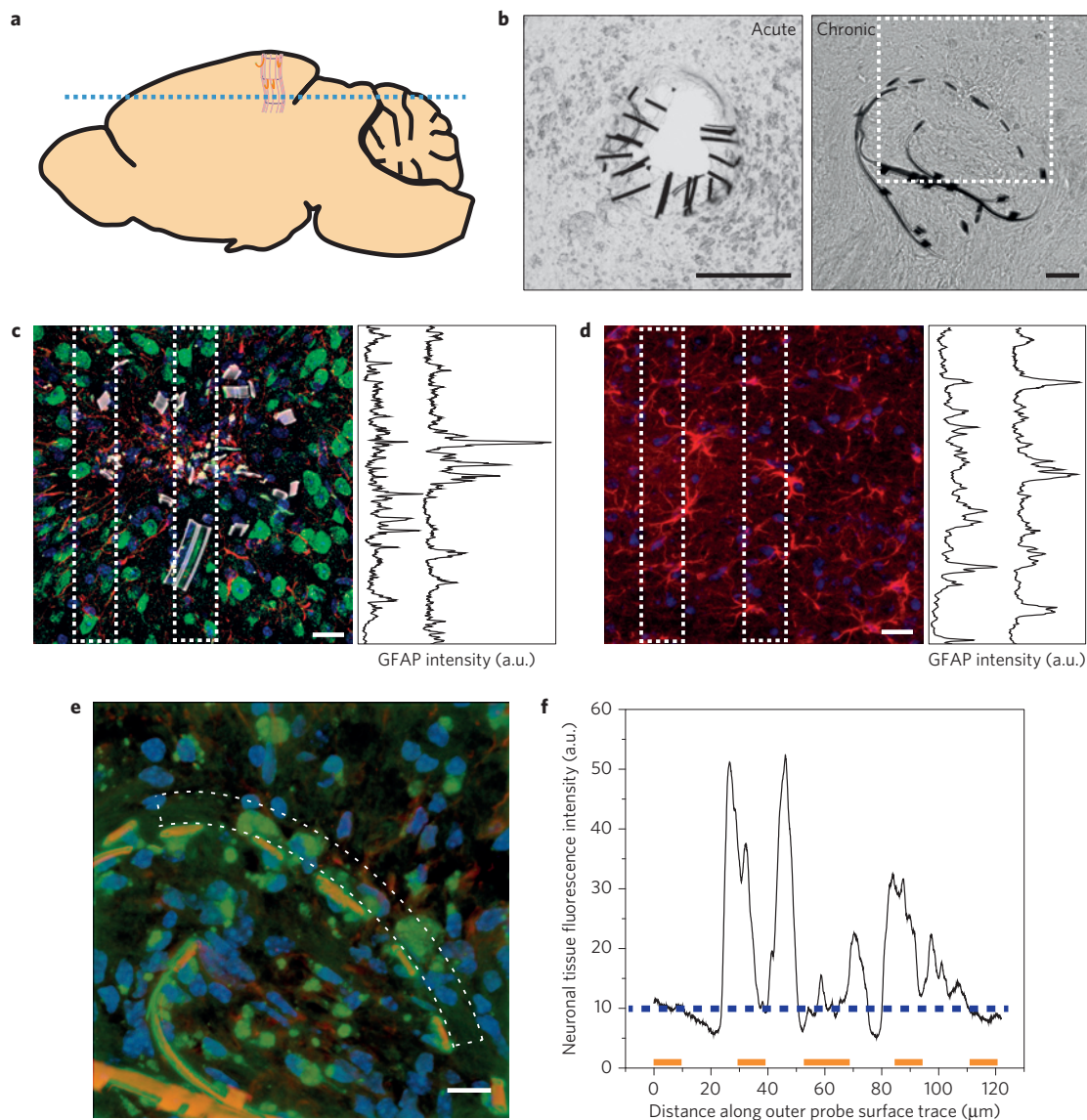
Figure 4 | Implanted macroporous nanoelectronic probe–tissue histology. a, Schematic of brain slice sample preparation. The blue dashed line indicates the slice direction perpendicular to the implanted macroporous probe. **b**, Bright-field images of the probe/tissue interface cross-section. The dark objects in the image are components of the probe. Left: Bright-field image of a 100-μm-thick acute slice. Scale bar, 100 μm. Right: Bright-field image of a 20-μm-thick cross-section slice five weeks after implantation. The white dashed box highlights the area imaged and shown in Fig. 4e. Scale bar, 20 μm. **c**, Projection of 3D reconstructed confocal micrograph of immunochemically labelled cross-section slice in right-side panel in **b** (five weeks post-implantation). The pseudo colour coding is as follows. Blue: nucleus, Hoechst; green: NeuN, labelling neuron nuclei; white: SU-8; and red: GFAP, specifically labelling reactive astrocytes. The fluorescent intensity profiles of the red channel (astrocyte) along the long axis of the two dashed box areas are plotted in the right panel. Scale bar, 20 μm. Similar data from a slice obtained about 150 μm deeper in the brain on this same probe is shown in Supplementary Fig. 8e. **d**, Immunochemical staining image of the control sample for **c** obtained from the contralateral hemisphere of the same mouse. The fluorescent intensity profiles of GFAP along the long axis of the two dashed box areas are plotted in the right panel. Scale bar, 20 μm. **e**, Projection of 3D reconstructed confocal micrograph of immunochemically labelled cross-section slice in **b**. The pseudo colour coding is as follows. Blue: nucleus, Hoechst; green: β-tubulin-III; orange: SU-8; and red: GFAP. Scale bar, 10 μm. **f**, Green channel (β-tubulin-III) fluorescence intensity plotted along the outer curved portion of the probe area outlined in the dashed area in **e**, from left to right. Orange bars indicate the positions of the mesh components. The blue dashed line indicates the average of the β-tubulin-III fluorescence intensity for the entire imaged area in **e**. All tissue slices were prepared post-implantation into the somatosensory cortex region of mice (Methods), as shown schematically in **a**.

(LFPs) in anaesthetized rats[40]. A spatial map of the recorded LFP is plotted in Supplementary Fig. 5a. The similarity and coherence between channels is consistent with the fact that the LFPs spread beyond[41] the dimension of the macroporous probe recording region, about 100 μm laterally and 1 mm vertically. Multiplexed recording experiments were conducted more than ten times using nanowire FET sensor probes, and all experiments resulted in >80% active sensor yield and similar recording performance in terms of potential

shapes and amplitude. In addition, probes with platinum electrode sensors implanted in the somatosensory cortex region of a mouse brain (Fig. 3d) exhibited sharp millisecond spikes. Standard data processing and spike sorting (Methods and Fig. 3e) yielded a uniform potential waveform with an average duration of 1.8 ms and a peak-to-peak amplitude of 172 μV, characteristic of single-unit action potentials. The high signal-to-noise ratio (>7) of the single-unit recording suggests a close proximity between the sensor and the

firing neurons[42], and thus provides at least comparable brain activity recordings to those of conventional probes[13], but with the advantage of being chronically much more biocompatible, as discussed below.

The chronic response of neural tissue to our ultra-flexible macroporous probes has been addressed through histology studies carried out five weeks post-implantation. A schematic of a macroporous probe inserted into the somatosensory cortex (Fig. 4a) highlights the perpendicular orientation (with respect to the implanted probe) at which the tissue was sectioned at different times post-implantation. In general, slices were prepared after fixing the brain tissue using standard procedures (Methods) without removing the ultra-flexible macroporous nanoelectronic probes. Comparison of bright-field optical images recorded from similar acute (Fig. 4b, left) and chronic 5-week post-implantation (Fig. 4b, right) tissue slices highlight several key points. First, the acute slice exhibits a tissue void within the interior of the roughly hollow cylindrical probe structure, which is consistent with ablation or displacement of tissue during implantation of the frozen probe. Second, images from the tissue 5-week post-implantation shows no void, thus indicating that cells and/or neural projections interpenetrate through the macroporous probe over time to fill the acute void. In addition, analysis of chronic images (dashed white box, Supplementary Fig. 8a) shows that at least some of the sensor arms can achieve the designed bend-out geometry post-implantation. This feature can facilitate positioning sensor devices away from any residual tissue damage resulting from implantation.

To evaluate more critically the chronic response of our macroporous nanoelectronic probes we used immunochemical staining[14] of cross-section slices containing our probes. Confocal microscopy images of a region including a macroporous probe (Fig. 4c) show a normal growth density of neuron cell bodies (NeuN) in close proximity, <50 μm, to the probe components (Supplementary Fig. 8d), although the soma density inside the probe cylinder is lower than outside. The close proximity of neuron cell bodies is in contrast to typical chronic observations reported for other types of neural probes[4,19,25,43], which we discuss further below. In addition, glial fibrillary acidic protein (GFAP) expression is slightly elevated at the centre of the probe, but not at the outer edge of the probe or surrounding region. Indeed, the spatial dependence of the GFAP signal encompassing this outer probe edge is similar to that in the control sample (Fig. 4d) prepared at the same time from the contralateral hemisphere without an implanted probe. These data suggest that the slightly elevated GFAP expression inside the probe cylinder is due to the acute tissue damage during implantation, and show, importantly, that our ultra-flexible macroporous probes do not elicit chronic immune response post-implantation.

To further characterize the robustness of these results and the details of the chronic distribution of neurons about the macroporous probe, we have stained tissue slices with β-tubulin-III, which can label both soma and neurites, from independent implantation experiments (Fig. 4e,f and Supplementary Fig. 8). Significantly, confocal microscopy images recorded five weeks post-implantation show no significant drop in β-tubulin-III expression inside (9.8 a.u., average) versus outside (10.2 a.u., average) the probe. These results suggest that neural projections, unlike somas, have sufficient mobility to interpenetrate and partially fill the central void produced during initial implantation. Moreover, analyses of the fluorescent intensity in the region immediately outside the probe (Fig. 4f and Supplementary Fig. 8c) show no sign of suppressed neuron growth immediately adjacent to the probe structural elements; indeed, these data indicate that the neuronal fluorescence signal within 10 μm of the probe components (20–50 a.u., average) is more than two to five times the value for neurons averaged over the entire image. In addition, measurements made from a tissue/probe slice 150 μm deeper in the brain than shown in Fig. 4c (Supplementary Fig. 8e)

and from an independent probe implant that partially collapsed during slow insertion (Supplementary Fig. 8f) exhibited similar results, and thus indicate that the macroporous probe structure is attractive to neurons (for example, neurophilic) and does not elicit the usual immune response. Similar results are observed in studies of syringe-injected mesh electronics[32], although conventional microwire[4,25] and silicon[19,43] neural probes as well as ultra-small but rigid[14] and flexible 2D polymer probes[16,17] show enhanced GFAP/astrocyte proliferation and a reduction of neuron density near these probe surface. As chronic failure of conventional brain probes involves neuronal loss and the encapsulation of non-neuronal cells such as astrocytes up to several hundred micrometres from the probe surface[4,43], our results suggest substantial benefits of the macroporous nanoelectronic probes for future chronic recording studies.

In summary, our 3D macroporous nanoelectronic probes, which feature both ultra-flexibility comparable to neural tissue and open structures with subcellular feature sizes allowing neuron interpenetration, represent a new strategy to merge 3D nanoelectronic devices with the neural circuits in the brain. We have shown that the ultra-flexible macroporous probes can be stereotaxically implanted in a frozen state into rodent brains with minimal surgical and acute tissue damage, and demonstrated the capability of recording multiplexed LFPs and single-unit action potentials from the somatosensory cortex. Significantly, chronic histology studies revealed unique characteristics, including a filling-in of neural tissue through the macroporous network and attractive neuron–probe interactions, which is in contrast to results from other solid and more rigid probe designs[19,20], and are consistent with a unique long-term stability and biocompatibility of the probe–tissue interface. Although it will be important in future studies to develop these probes further, for example by extending the chronic histology studies to shorter and longer times, and increasing the number of sensor elements available for multiplexed recording and/or introducing stimulation capabilities, we believe the present chronic histology and acute recording studies already show the unique advantages of our ultra-flexible 3D macroporous electronic probes and indicate the importance of exploring the stability of chronic neural activity mapping and implants for next-generation brain–machine interfaces in the near future.

Methods

Methods and any associated references are available in the online version of the paper.

References

1. Alivisatos, A. P. et al. Neuroscience. The brain activity map. Science **339,** 1284–1285 (2013).
2. Birmingham, K. et al. Bioelectronic medicines: A research roadmap. Nature Rev. Drug Discov. **13,** 399–400 (2014).
3. Shen, H. Neurotechnology: BRAIN storm. Nature **503,** 26–28 (2013).
4. Polikov, V. S., Tresco, P. A. & Reichert, W. M. Response of brain tissue to chronically implanted neural electrodes. J. Neurosci. Methods **148,** 1–18 (2005).
5. Olsen, S. R., Bortone, D. S., Adesnik, H. & Scanziani, M. Gain control by layer six in cortical circuits of vision. Nature **483,** 47–52 (2012).
6. Mizuseki, K., Diba, K., Pastalkova, E. & Buzsaki, G. Hippocampal CA1 pyramidal cells form functionally distinct sublayers. Nature Neurosci. **14,** 1174–1181 (2011).
7. Hochberg, L. R. et al. Reach and grasp by people with tetraplegia using a neurally controlled robotic arm. Nature **485,** 372–375 (2012).
8. Nicolelis, M. A. Actions from thoughts. Nature **409,** 403–407 (2001).
9. Taylor, D. M., Tillery, S. I. & Schwartz, A. B. Direct cortical control of 3D neuroprosthetic devices. Science **296,** 1829–1832 (2002).
10. Perlmutter, J. S. & Mink, J. W. Deep brain stimulation. Annu. Rev. Neurosci. **29,** 229–257 (2006).
11. Seymour, J. P. & Kipke, D. R. Neural probe design for reduced tissue encapsulation in CNS. Biomaterials **28,** 3594–3607 (2007).

1291

12. Kozai, T. D. & Kipke, D. R. Insertion shuttle with carboxyl terminated self-assembled monolayer coatings for implanting flexible polymer neural probes in the brain. *J. Neurosci. Methods* **184,** 199–205 (2009).
13. HajjHassan, M., Chodavarapu, V. & Musallam, S. NeuroMEMS: Neural Probe Microtechnologies. *Sensors* **8,** 6704–6726 (2008).
14. Kozai, T. D. *et al.* Ultrasmall implantable composite microelectrodes with bioactive surfaces for chronic neural interfaces. *Nature Mater.* **11,** 1065–1073 (2012).
15. Seymour, J. P. & Kipke, D. R. Fabrication of polymer neural probes with sub-cellular features for reduced tissue encapsulation. *Conf. Proc. IEEE Eng. Med. Biol. Soc.* **1,** 4606–4609 (2006).
16. Kim, T. I. *et al.* Injectable, cellular-scale optoelectronics with applications for wireless optogenetics. *Science* **340,** 211–216 (2013).
17. Sohal, H. S. *et al.* The sinusoidal probe: A new approach to improve electrode longevity. *Front. Neuroeng.* **7,** 10 (2014).
18. Nicolelis, M. A. *et al.* Chronic, multisite, multielectrode recordings in macaque monkeys. *Proc. Natl Acad. Sci. USA* **100,** 11041–11046 (2003).
19. Rousche, P. J. & Normann, R. A. Chronic recording capability of the Utah Intracortical Electrode Array in cat sensory cortex. *J. Neurosci. Methods* **82,** 1–15 (1998).
20. Kipke, D. R., Vetter, R. J., Williams, J. C. & Hetke, J. F. Silicon-substrate intracortical microelectrode arrays for long-term recording of neuronal spike activity in cerebral cortex. *IEEE Trans. Neural Syst. Rehabil. Eng.* **11,** 151–155 (2003).
21. Miller, K., Chinzei, K., Orssengo, G. & Bednarz, P. Mechanical properties of brain tissue *in-vivo*: Experiment and computer simulation. *J. Biomech.* **33,** 1369–1376 (2000).
22. Perge, J. A. *et al.* Intra-day signal instabilities affect decoding performance in an intracortical neural interface system. *J. Neural Eng.* **10,** 036004 (2013).
23. Biran, R., Martin, D. C. & Tresco, P. A. The brain tissue response to implanted silicon microelectrode arrays is increased when the device is tethered to the skull. *J. Biomed. Mater. Res. A* **82,** 169–178 (2007).
24. Dickey, A. S., Suminski, A., Amit, Y. & Hatsopoulos, N. G. Single-unit stability using chronically implanted multielectrode arrays. *J. Neurophysiol.* **102,** 1331–1339 (2009).
25. Jackson, A. & Fetz, E. E. Compact movable microwire array for long-term chronic unit recording in cerebral cortex of primates. *J. Neurophysiol.* **98,** 3109–3118 (2007).
26. Tee, B. C., Wang, C., Allen, R. & Bao, Z. An electrically and mechanically self-healing composite with pressure- and flexion-sensitive properties for electronic skin applications. *Nature Nanotech.* **7,** 825–832 (2012).
27. Mannoor, M. S. *et al.* 3D printed bionic ears. *Nano Lett.* **13,** 2634–2639 (2013).
28. Jeong, J. W. *et al.* Soft materials in neuroengineering for hard problems in neuroscience. *Neuron* **86,** 175–186 (2015).
29. Spira, M. E. & Hai, A. Multi-electrode array technologies for neuroscience and cardiology. *Nature Nanotech.* **8,** 83–94 (2013).
30. Kruskal, P. B., Jiang, Z., Gao, T. & Lieber, C. M. Beyond the patch clamp: Nanotechnologies for intracellular recording. *Neuron* **86,** 21–24 (2015).
31. Tian, B. *et al.* Macroporous nanowire nanoelectronic scaffolds for synthetic tissues. *Nature Mater.* **11,** 986–994 (2012).
32. Liu, J. *et al.* Syringe-injectable electronics. *Nature Nanotech.* **10,** 629–636 (2015).
33. Liu, J. *et al.* Multifunctional three-dimensional macroporous nanoelectronic networks for smart materials. *Proc. Natl Acad. Sci. USA* **110,** 6694–6699 (2013).
34. Lee, H., Bellamkonda, R. V., Sun, W. & Levenston, M. E. Biomechanical analysis of silicon microelectrode-induced strain in the brain. *J. Neural Eng.* **2,** 81–89 (2005).
35. Rousche, P. J. *et al.* Flexible polyimide-based intracortical electrode arrays with bioactive capability. *IEEE Trans. Biomed. Eng.* **48,** 361–371 (2001).
36. du Roure, O. *et al.* Force mapping in epithelial cell migration. *Proc. Natl Acad. Sci. USA* **102,** 2390–2395 (2005).
37. Sharp, A. A., Ortega, A. M., Restrepo, D., Curran-Everett, D. & Gall, K. *In vivo* penetration mechanics and mechanical properties of mouse brain tissue at micrometer scales. *IEEE Trans. Biomed. Eng.* **56,** 45–53 (2009).
38. Petersen, C. C. The functional organization of the barrel cortex. *Neuron* **56,** 339–355 (2007).
39. Boulton, A. A., Baker, G. B. & Vanderwolf, C. H. *Neurophysiological Techniques* (Humana Press, 1990).
40. Sheeba, J. H., Stefanovska, A. & McClintock, P. V. Neuronal synchrony during anesthesia: A thalamocortical model. *Biophys. J.* **95,** 2722–2727 (2008).
41. Kajikawa, Y. & Schroeder, C. E. How local is the local field potential? *Neuron* **72,** 847–858 (2011).
42. Stratton, P. *et al.* Action potential waveform variability limits multi-unit separation in freely behaving rats. *PLoS ONE* **7,** e38482 (2012).
43. Biran, R., Martin, D. C. & Tresco, P. A. Neuronal cell loss accompanies the brain tissue response to chronically implanted silicon microelectrode arrays. *Exp. Neurol.* **195,** 115–126 (2005).

Acknowledgements

Author contributions
C.X., J.L. and C.M.L. conceived the idea and designed the experiments. C.X., J.L., T.-M.F., X.D. and W.Z. performed the experiments and analyses. C.X. and C.M.L. wrote the manuscript. All authors discussed the results, interpreted the findings and reviewed the manuscript.

Additional information
Supplementary information is available in the online version of the paper. Reprints and permissions information is available online at www.nature.com/reprints. Correspondence and requests for materials should be addressed to C.M.L.

Competing financial interests
The authors declare no competing financial interests.

Methods

Macroporous nanoelectronic brain probe preparation. Macroporous nanoelectronic probes were fabricated using methods described previously[18,27] (see Supplementary Methods for details). In brief, the 2D probe structure was fabricated using photolithography on a nickel metal release layer deposited on a silicon substrate (600 nm SiO₂ or 100 nm SiO₂/200 nm Si₃N₄, n-type 0.005 V cm, Nova Electronic Materials, Flower Mound). After fabrication, a custom-designed PCB connector was mounted on the silicon substrate next to the contact region of the probe. Connections from the contact pads to the connector were made by wire bonding. Subsequently, the relief region of the probe was soaked in nickel etchant (TFB, Transene Company) for 60–120 min at 25 °C to release the free-standing portion of the probe, whereas the remainder of the probe is attached to the substrate. The substrate was trimmed to the size of the contact region before implantation.

Stereotaxic surgery and probe implantation. The macroporous nanoelectronic brain probe implantation was carried following a standard rodent stereotaxic surgery protocol. Briefly, the rat or mouse was anaesthetized with intraperitoneally administered ketamine/xylazine (Patterson Veterinary Supply), and held in a stereotaxic frame (Lab Standard Stereotaxic Instrument, Stoelting). A hole in the cranium (6 mm × 6 mm) was milled with a dental drill (Micromotor with On/Off Pedal 110/220, Grobet USA) above the somatosensory cortex area. The dura was incised and resected. The probe was then implanted stereotaxically in the frozen state. Acute recording was performed 0.5–2 h after the implantation. For chronic experiments, the surgical closure and probe connector fixture on the skull were achieved with C&B-METABOND (Cement System, Parkell). Anti-inflammatory and anti-bacterial ointment was swabbed onto the skin after surgery. A 0.3 ml intraperitoneal injection of Buprenex (Patterson Veterinary Supply, diluted with 0.5 ml of PBS) for 0.1 mg kg⁻¹ was administered to reduce postoperative pain. Animals were observed for 4 h after surgery and hydrogel was provided for food and water, with a heating pad at 37 °C for the remainder of postoperative care. All animal procedures conformed to US National Institutes of Health guidelines and were approved by Harvard University's Animal Care and Use Committee.

Incubation and behavioural analysis. Animals were cared every day for three days after the surgery and every other day after the first three days. Animals were administered 0.3 ml of Buprenex (0.1 mg kg⁻¹, diluted with 0.5 ml 1× PBS) every 12 h for three days. Animals were also observed every other day for behavioural changes. The room was maintained at constant temperature on a 12–12 h light–dark cycle.

Voltage sensing using the nanowire FET sensors and Pt electrodes. Nanowire device recording was carried out with a custom-built 100 mV d.c. voltage source,

and the current was amplified with a custom-built 16-channel current/voltage preamplifier with a typical gain setting of 10⁶ A/V. The signals were filtered with a 3 kHz low-pass filter (CyberAmp 380, Molecular Devices), digitized at a sampling rate of 20 kHz (AxonDigi1440A, Molecular Devices) and recorded using Clampex 10 software (Molecular Devices). The measured conductance changes of nanowire devices were translated to potential according to calibration curves measured after implantation[33]. All nanowire devices were tested for functionality before recording. Voltage signals from Pt electrode sensors were recording using a 32-channel Intan RHD 2132 amplifier evaluation system (Intan Technologies LLC.) with an Ag/AgCl electrode acting as the reference and counter electrode. The sampling rate was 20 kHz, and a 300–6,000 Hz band-pass filter was applied for single-unit recording. Spike sorting was performed using Clampfit (Molecular Devices). The impedance of the Pt electrodes was measured using the same equipment. The a.c. leakage impedance of the probe components was measured by means of a B1500A semiconductor parameter analyser (Keysight).

Histology sample preparation. After anaesthesia (described above) was introduced, the animal was perfused transcardially with PBS and then 40 ml 4% paraformaldehyde (Sigma-Aldrich). The animal was decapitated and the brain was removed from the skull and set in 4% formaldehyde for 24 h as post fixation. The brain was then transferred to incrementally increasing sucrose solutions (10–30%) (Sigma-Aldrich) for cryoprotection, followed by sectioning into 10–150 μm slices perpendicular or parallel to the probe using a Leica CM1950 cryostat (Leica Microsystems). The slices were pre-blocked and permeabilized (0.2–0.25% Triton X-100 and 1% bovine serum albumin (BSA) in PBS, (Sigma-Aldrich)) for 1 h at room temperature. Next the slices were incubated with primary antibodies containing 0.2% triton and 3% serum overnight at 4 °C, then incubated with the secondary antibodies with fluorophores overnight at 4 °C. For counter-staining of cell nuclei, cells were incubated with 0.1–1 μg ml⁻¹ Hoechst 34580 (Invitrogen) for 1 min.

Reagents used for different cell types are as follows (all from AbCam). *Neuron*: Rabbit polyclonal to NeuN and Rabbit polyclonal to β-tubulin-III were used as primary antibodies. Goat anti-rabbit IgG AlexaFlour 488 was used as the second antibody. *Astrocyte*: Chicken polyclonal to GFAP and Goat anti-chicken IgG alexaFlour 647 were used as the primary and secondary antibodies, respectively.

Structural and fluorescent imaging. Bright-field, dark-field and confocal fluorescent micrographs of samples were acquired on an Olympus BX61 microscope (Olympus America) or a Zeiss LSM 780 confocal microscope (Carl Zeiss Microscopy). Confocal images were acquired using 405, 473, 559 and 635 nm wavelength lasers as excitation and a spectrum detector collecting emission. ImageJ (ver. 1.45i, Wayne Rasband, National Institutes of Health) or Zen (Carl Zeiss Microscopy) was used for analysis of the image data.